

# Full-Duplex OFDM Radar With LTE and 5G NR Waveforms: Challenges, Solutions, and Measurements

Carlos Baquero Barneto<sup>✉</sup>, Student Member, IEEE, Taneli Riihonen<sup>✉</sup>, Member, IEEE, Matias Turunen, Lauri Anttila<sup>✉</sup>, Member, IEEE, Marko Fleischer, Kari Stadius<sup>✉</sup>, Member, IEEE, Jussi Ryyynänen<sup>✉</sup>, Senior Member, IEEE, and Mikko Valkama<sup>✉</sup>, Senior Member, IEEE

**Abstract**—This article studies the processing principles, implementation challenges, and performance of orthogonal frequency-division multiplexing (OFDM)-based radars, with particular focus on the fourth-generation Long-Term Evolution (LTE) and fifth-generation (5G) New Radio (NR) mobile networks’ base stations and their utilization for radar/sensing purposes. First, we address the problem stemming from the unused subcarriers within the LTE and NR transmit signal passbands and their impact on frequency-domain radar processing. In particular, we formulate and adopt a computationally efficient interpolation approach to mitigate the effects of such empty subcarriers in the radar processing. We evaluate the target detection and the corresponding range and velocity estimation performance through computer simulations and show that high-quality target detection as well as high-precision range and velocity estimation can be achieved. In particular, 5G NR waveforms, through their impressive channel bandwidths and configurable subcarrier spacing, are shown to provide very good radar/sensing performance. Then, a fundamental implementation challenge of transmitter-receiver (TX–RX) isolation in OFDM radars is addressed, with specific emphasis on shared-antenna cases, where the TX–RX isolation challenges are the largest. It is confirmed that from the OFDM radar processing perspective, limited TX–RX isolation is primarily a concern in the detection of static targets, while moving targets are inherently more robust to transmitter self-interference (SI). Properly tailored analog/RF and digital SI cancellation solutions for OFDM radars are also described and

implemented and shown through RF measurements to be key technical ingredients for practical deployments, particularly from static and slowly moving targets’ point of view.

**Index Terms**—Analog cancellation, digital cancellation, 5G New Radio (NR), in-band full-duplex, joint communications and sensing, Long-Term Evolution (LTE), orthogonal frequency-division multiplexing (OFDM), radar, RF convergence, self-interference (SI).

## I. INTRODUCTION

MANY emerging technologies and applications demand higher and higher communications capacity and bandwidth, while the importance of various radio-based sensing schemes is also continuously increasing in commercial, industrial, and military fields [1], [2]. Good examples, where both radio communications and sensing are of high importance, are autonomous cars, or the automotive sector overall, flight control systems, as well as medical sensors and monitoring [3]–[5], to name but a few. Although classically radio communications and radio-based sensing systems are designed, developed, and deployed completely independently of each other, the congestion of the available radio spectrum has started to raise interest in merging these functionalities and systems to shared frequency bands and potentially even to same hardware platforms. This is commonly referred to as RF convergence in the literature, with comprehensive state-of-the-art surveys being available in [1] and [2].

The integrated or joint operation of communications and radar systems implies that the same waveform is utilized for both tasks. It is generally well known that orthogonal frequency-division multiplexing (OFDM) waveforms are very well suited for radio communications, providing robustness against multipath fading, facilitating adaptive modulation and coding across subcarriers, as well as offering high flexibility in radio system design and radio resource management. In addition, the use of OFDM-based waveforms for sensing/radar purposes is receiving increasing interest as described in [1], [3], [4], and [6]–[12]. Relatively recently, in [9], [13], and [14], a certain level of convergence of mobile communication networks and radar systems was addressed, with a specific focus on the use of the Long-Term Evolution (LTE) network downlink reference and synchronization signals for passive radar purposes. In addition, in [15], the use of 5G-grade

Manuscript received March 14, 2019; revised May 22, 2019 and June 24, 2019; accepted July 8, 2019. Date of publication August 19, 2019; date of current version October 4, 2019. This work was supported in part by the Academy of Finland under Grant #288670, Grant #301820, Grant #310991, and Grant #315858, in part by Nokia Bell Labs, in part by the Doctoral School of Tampere University, and in part by the Finnish Funding Agency for Innovation through the “RF Convergence” Project. This article is an expanded version from the IEEE MTT-S Radio and Wireless Week [Radio and Wireless Symposium (RWS)], Orlando, FL, USA, January 20–23, 2019. (*Corresponding author: Mikko Valkama*)

C. Baquero Barneto, T. Riihonen, M. Turunen, L. Anttila, and M. Valkama are with the Unit of Electrical Engineering, Tampere University, 33100 Tampere, Finland (e-mail: mikko.e.valkama@tut.fi).

M. Fleischer is with Nokia Mobile Networks, D-89081 Ulm, Germany.

K. Stadius and J. Ryyynänen are with the School of Electrical Engineering, Aalto University, 02150 Espoo, Finland.

This article has supplementary downloadable material available at <http://ieeexplore.ieee.org>, provided by the authors. This includes a video that illustrates tracking the distances and speeds of moving cars by using the developed OFDM radar concept. Sequences of radar images are shown, with RF cancellation only and with both RF and digital cancellation. This material is 0.725 MB in size.

Color versions of one or more of the figures in this article are available online at <http://ieeexplore.ieee.org>.

Digital Object Identifier 10.1109/TMTT.2019.2930510

phased-array hardware for radar purposes is investigated, however, in the context of a classical frequency-modulated continuous-wave (FMCW) waveform.

In this article, building on our initial work in [10], we also focus on mobile networks, particularly time-division duplexing (TDD)-based LTE and 5G New Radio (NR) systems [16], and the use of the corresponding downlink transmit signals for radar/sensing purposes. We first assume that there is sufficient TX–RX isolation in LTE and NR base stations, referred to as eNB and gNB, respectively, such that when viewed from the sensing point of view, they can essentially act as monostatic radars and thus utilize the complete downlink waveforms for radar processing. We then deploy frequency-domain radar processing, similar to [4], while putting specific emphasis on the exact frequency-domain structure of the LTE and NR downlink signals over multiple subframes, potentially up to a complete radio frame of 10 ms [17], [18]. We specifically address the impact of null/unused subcarriers within the transmit signal passband of various OFDM symbols in the LTE and NR radio frames and develop a time–frequency interpolation type of an approach to reduce their effects in the radar processing.

Then, we address a fundamental implementation challenge stemming from the limited TX–RX isolation [11], [19]–[22] in real base stations and the corresponding transmitter self-interference (SI) at the radar. Our main emphasis is on the challenging monostatic scenario where the same antenna system of the eNB/gNB is shared between the TX and RX, building, e.g., on a circulator [20], [23]–[25] or an electrical balance duplexer (EBD) [12], [26], [27]. We first observe that from the perspective of OFDM radar processing, the transmitter SI is most problematic for static target detection, while moving targets are already more robust. Then, to enhance the limited TX–RX isolation, properly tailored RF and digital cancellation solutions are devised to suppress the SI, without suppressing the actual target reflections. Practical RF measurement results are then also reported, incorporating the developed cancellation solutions, demonstrating the proper operation as well as the target detection and range–velocity estimation capabilities of the overall LTE/NR radar system for both static and moving targets.

Overall, compared to our initial work in [10] and other existing literature, we have substantially extended the technical scope and contributions by taking the fundamental TX–RX isolation and associated SI issue in monostatic OFDM radars into account. We also provide technical solutions and corresponding RF measurement results to relax or solve the SI challenge while also incorporating the timely 5G NR aspects at waveform and physical layer processing level.

For clarity, it is acknowledged that TX–RX isolation is basically a known challenge in all continuous-wave radar systems, and that sufficient RF isolation is always needed to prevent receiver saturation [2], [12], [26], [28]. From the actual radar processing point of view, however, FMCW-type of constant-envelope radars [29]–[31] can largely suppress the remaining SI through down-mixing with the modulated transmit waveform in the receive path [29], [30]. In monostatic

OFDM radars, such an approach is not possible but actual cancellation processing is required. We also note that the time-domain digital cancellation solutions described and experimented in this article are complementary methods, compared to radar-domain direct interference and clutter suppression techniques described in [32]–[34].

Finally, we also acknowledge that an alternative approach to facilitate sensing/radar capabilities in base stations is to deploy a separate radar transceiver system, e.g., FMCW-based, with appropriate coexistence measures with the communications transceiver. However, in this article, we do not pursue such direction but focus on the use of the LTE/NR base station itself for radar purposes, while sending the regular standard-compliant downlink communications waveform, and on the related signal processing aspects and the TX–RX isolation challenge, with particular emphasis on the scenario where the same antenna system is shared by the TX and RX.

The rest of this article is organized as follows. In Section II, the considered OFDM radar system model is described, incorporating the frequency-domain radar processing based on 3GPP LTE and NR specifications-compliant transmit waveforms. In addition, the achievable target detection and the associated range and velocity estimation performances are assessed in an ideal SI-free reference scenario. Then, in Section III, the limited TX–RX isolation and the associated SI challenge are addressed, and proper cancellation solutions are developed. Section IV provides the description of the RF measurement system, obtained results, and their analysis. Finally, Section V concludes this article.

## II. OFDM RADAR: SYSTEM MODEL AND REFERENCE PERFORMANCE

### A. System Model and Basic Subcarrier Processing

The radar functionality is pursued in an LTE or NR network base-station unit by utilizing the known transmit waveform together with frequency-domain radar processing as shown in Fig. 1. The radar processing seeks to detect targets surrounding the eNB/gNB by using the known samples within the LTE or NR frequency-domain resource grid over multiple OFDM symbols, denoted by  $\mathbf{X}$ . This grid contains frequency-domain samples corresponding to the overall composite transmit waveform, thus comprising all the downlink physical and logical channels and reference signals as specified in [17] for LTE and in [18] for NR. The size of the grid or matrix  $\mathbf{X}$  is  $S \times R$  where  $S$  denotes the number of active subcarriers, while  $R$  indicates the number of OFDM symbols considered in the radar processing.

In the transmitter processing, the time-domain waveform is generated through blockwise IFFT operating on  $\mathbf{X}$ , together with cyclic prefix addition, as described in [17] and [18]. The radiated transmit waveform will then interact with one or multiple targets, producing reflections that will be captured by the receiving system. For simplicity, perfect isolation between the transmit and receive systems is assumed in this section, while the limited TX–RX isolation aspects and the associated SI challenge are addressed in Section III. The received signal

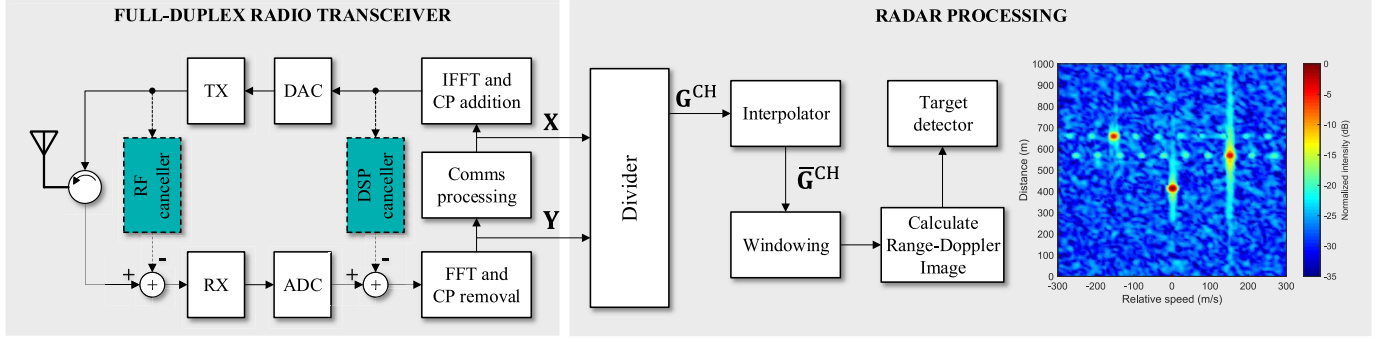


Fig. 1. Block diagram of the considered OFDM radar building on regular LTE or NR downlink transmission and frequency-domain radar processing. All communication-related digital waveform processing takes place inside the “Comms processing” box.

containing the target reflections is demodulated and processed through fast Fourier transform (FFT) to obtain the corresponding receive grid, denoted by  $\mathbf{Y}$ .

The distance and the relative speed of a single target correspond to a propagation delay  $\tau_k$  and a Doppler shift  $f_{D,k}$ , respectively. With  $K$  point targets or reflections, the receive grid sample on  $p$ th row and  $q$ th column, i.e.,  $Y_{p,q} = (\mathbf{Y})_{p,q}$  can be expressed as [4], [10]

$$Y_{p,q} = \sum_{k=0}^{K-1} b_k X_{p,q} e^{2\pi j (q T_s f_{D,k} - p \tau_k \Delta f)} + N_{p,q} \quad (1)$$

where  $X_{p,q} = (\mathbf{X})_{p,q}$ ,  $N_{p,q}$  corresponds to receiver thermal noise sample, while  $b_k$  models the effective attenuation factor of the  $k$ th reflection. Furthermore, the subcarrier spacing and the total OFDM symbol duration (including the cyclic prefix of length  $T_{cp}$ ) are denoted by  $\Delta f$  and  $T_s = 1/\Delta f + T_{cp}$ , respectively. In general, the propagation delay causes different phase shifts for different subcarriers, which can be used to estimate the range of each target. Similarly, the Doppler shift produces different phase shifts for the different OFDM symbols that can be utilized to compute the relative speeds of the targets.

The actual radar processing building on the known transmit waveform can be implemented in multiple ways [28], [35], either with time-domain or subcarrier-domain processing. In this work, similar to [3]–[6], [11], and [36], we adopt subcarrier-domain processing utilizing directly the transmit and receive grids of samples, i.e.,  $\mathbf{X}$  and  $\mathbf{Y}$ , respectively. For the classical matched filtering-based approach [28], represented at OFDM symbol level, a new processed matrix  $\mathbf{G}$  can be defined as  $\mathbf{G}^{\text{MF}} = \mathbf{Y} \odot \mathbf{X}^*$ , where  $\odot$  refers to elementwise (Hadamard) product, while the superscript  $(\cdot)^*$  denotes complex conjugation. Alternatively, the reflection channel estimation-like scheme, utilized also in [3], [4], [6], and [11], reads  $\mathbf{G}^{\text{CH}} = \mathbf{Y} \oslash \mathbf{X}$ , where  $\oslash$  denotes element-wise division.

Based on (1), when interpreted at an individual subcarrier  $p$  of an OFDM symbol  $q$ , we can write  $G_{p,q}^{\text{MF}} = (\mathbf{G}^{\text{MF}})_{p,q}$  as

$$G_{p,q}^{\text{MF}} = Y_{p,q} X_{p,q}^* = \sum_{k=0}^{K-1} b_k |X_{p,q}|^2 e^{2\pi j (q T_s f_{D,k} - p \tau_k \Delta f)} + \tilde{N}_{p,q}^{\text{MF}} \quad (2)$$

while the corresponding expression for  $G_{p,q}^{\text{CH}} = (\mathbf{G}^{\text{CH}})_{p,q}$  reads

$$G_{p,q}^{\text{CH}} = \frac{Y_{p,q}}{X_{p,q}} = \sum_{k=0}^{K-1} b_k e^{2\pi j (q T_s f_{D,k} - p \tau_k \Delta f)} + \tilde{N}_{p,q}^{\text{CH}} \quad (3)$$

where  $\tilde{N}_{p,q}^{\text{MF}}$  and  $\tilde{N}_{p,q}^{\text{CH}}$  denote processed noise samples. Although the matched filter is known [28], [35] to optimize the signal-to-noise ratio (SNR) from an individual target or reflection point of view, the noiseless range and velocity profiles stemming from (2) are clearly data-dependent. Instead, the noiseless component in (3) building on the channel estimation approach is data-independent. In addition, as discussed in [3] and [6], correlator or matched filter-based processing can have some drawbacks related to range profile sidelobes and, thus, potentially more limited dynamic range in scenarios with multiple targets. This is inline with the ambiguity function [35]-based analysis carried out in [9] and [14] for OFDM signals. Hence, in the rest of this article, similar to [3], [4], [6], and [11], we follow the channel estimationlike approach and assume that the subcarrier-level preprocessing is carried out as defined in (3).

### B. Interpolation, Target Detection, and Range–Velocity Estimation

For fixed  $p$  and varying  $q$ , the samples of  $G_{p,q}^{\text{CH}}$  correspond to a sum of complex exponentials with oscillating frequencies being defined by the Doppler shifts and, thus, the target velocities. Similarly, if  $q$  is fixed while  $p$  varies, we again obtain a sum of complex exponentials but now the frequencies are defined by the propagation delays and, thus, the target distances. These facilitate both target detection as well as velocity and range estimation, as defined in the following. However, the LTE and NR transmit grids contain unused subcarriers within the transmit signal passband, whose locations also vary from OFDM symbol to another [17], [18]. The direct calculation of (3) is therefore not feasible in these points, but it is carried out only for the active subcarriers. Then, to deal with the missing samples prior to the actual target detection and range–velocity estimation, the proposed LTE/NR-compliant radar processing includes appropriate interpolation along either  $p$  or  $q$  domain.

Stemming from the more detailed structure of the LTE and NR grids [17], [18], we adopt linear interpolation across OFDM symbols and, thus, define the interpolated grid sample  $\bar{G}_{p,q}^{\text{CH}}$  at an unused subcarrier  $p$  of an OFDM symbol  $q$  as

$$\bar{G}_{p,q}^{\text{CH}} = G_{p,q_1}^{\text{CH}} + \left( \frac{G_{p,q_2}^{\text{CH}} - G_{p,q_1}^{\text{CH}}}{q_2 - q_1} \right) (q - q_1) \quad (4)$$

where  $q_1 < q < q_2$  and the subcarrier  $p$  is assumed active at OFDM symbols  $q_1$  and  $q_2$ . In the rest of this article, we use systematically the notation of the interpolated grid, i.e.,  $\bar{G}_{p,q}^{\text{CH}}$ , while naturally at the active subcarriers  $\bar{G}_{p,q}^{\text{CH}} = G_{p,q}^{\text{CH}}$ .

In this work, the target detection and range–velocity estimation build on the range–Doppler profile calculated by using the interpolated grid. One common approach [36] is to calculate the radar image through the periodogram, expressed as

$$A(s, r) = \left| \sum_{q=0}^{R'-1} \left( \sum_{p=0}^{S'-1} \bar{G}_{p,q}^{\text{CH}} W_{p,q} e^{j2\pi \frac{ps}{S'}} \right) e^{-j2\pi \frac{qr}{R'}} \right|^2 \quad (5)$$

where the inner IFFTs of size  $S' \geq S$  yield OFDM symbol-wise range profiles, while the outer FFTs of size  $R' \geq R$  correspond to velocity profiles. Importantly, the ranges of  $s$  and  $r$  over which the transforms are calculated can be limited to chosen feasible distances and velocities, respectively. These are denoted in the following by  $S_{\text{MAX}}$  and  $R_{\text{MAX}}$ , while the corresponding set of periodogram indices is denoted by  $\Omega_A$ . The periodogram in (5) also includes sets of additional weights  $W_{p,q}$ , which correspond to windowing of the interpolated grid in order to control the sidelobe levels [36].

In the actual target detector, the periodogram is subject to a threshold test [28], [35], expressed as

$$A(s, r) \stackrel{H_0}{\leqslant} T_{\text{th}} \quad (6)$$

where  $(s, r) \in \Omega_A$ ,  $T_{\text{th}}$  denotes the detection threshold,  $H_0$  refers to the null hypothesis (no target, noise only), while  $H_1$  refers to the alternative hypothesis (a target present). Specifically, if  $A(s, r) > T_{\text{th}}$ , the detector declares that the target is present, while if  $A(s, r) < T_{\text{th}}$ , it declares that the target is absent. We then denote the probability that  $A(s, r) > T_{\text{th}}$ , under  $H_0$  being true, by  $P_{\text{FA}}$ . The corresponding total false-alarm probability in the whole search space  $\Omega_A$  then reads  $P_{\text{FA,tot}} = 1 - (1 - P_{\text{FA}})^{|\Omega_A|}$  where  $|\Omega_A|$  refers to the size of  $\Omega_A$ . As shown in [4] and [28], assuming Gaussian-distributed receiver noise, the detection threshold  $T_{\text{th}}$  can be straightforwardly calculated to fix  $P_{\text{FA,tot}}$  to a chosen value, commonly known as the constant false-alarm rate (CFAR) detector.

In the case of the threshold test declaring that a target is present, the estimation of the target range and velocity can be pursued [28], [35]. Considering, for presentation simplicity, the single-target scenario, it is shown in [36] that the location of the peak of the periodogram is the corresponding maximum likelihood estimator, that is,

$$(\hat{s}, \hat{r}) = \arg \max_{(s, r) \in \Omega_A} A(s, r). \quad (7)$$

TABLE I

BASIC FEATURES AND OFDM RADAR PARAMETERS FOR THE CONSIDERED LTE AND NR CHANNEL BANDWIDTHS AT 3.5 GHz

	LTE 20	NR 20	NR 40	NR 100
Passband width (MHz)	18	19.08	38.16	98.28
Subcarrier spacing $\Delta f$ (kHz)	15	15	30	30
Cyclic prefix length, $T_{\text{cp}}$ ( $\mu$ s)	4.7	4.7	2.3	2.3
Active subcarriers, $S$	1200	1272	1272	3276
OFDM symbols, $R$	140	140	280	280
Bandwidth utilization (%)	90	95.4	95.4	98.28
Distance resolution (m)	8.3	7.9	3.9	1.5
Maximum distance (m)	700	700	350	350
Velocity resolution (m/s)	4.2	4.2	4.2	4.2
Maximum velocity (m/s)	$\pm 64$	$\pm 64$	$\pm 128$	$\pm 128$

To improve the resolution beyond the basic pixel size of the range–Doppler map, different interpolation-type peak refinement methods can be adopted as discussed in [4]. For generality, we note that the periodogram-based approach in (5) is only one feasible approach to create test statistics for target detection, while alternative methods can also be pursued.

### C. Reference Performance With LTE/NR Carriers

Simulations are next carried out to evaluate the performance of the interpolated periodogram-based OFDM radar described in Section II-B and to compare the LTE and NR waveforms and their feasibility for high-precision range and velocity estimation. In the evaluations, LTE and NR waveforms with carrier bandwidth of 20 MHz and subcarrier spacing of 15 kHz are considered as the baseline. In addition, NR waveforms with 30 kHz subcarrier spacing and carrier bandwidths of 40 and 100 MHz are also adopted. Assuming a downlink transmit radio frame of 10 ms [17], [18] and the above radio interface numerologies, the main OFDM radar parameters are summarized in Table I.

The assumed network center frequency is  $f_c = 3.5$  GHz, and all the main downlink physical channels and signals, such as PSS, SSS, CRS, DMRS, CSI-RS, PRS, PDSCH, PDCCH, PCFICH, PHICH, and PBCH, are modeled in both LTE and NR sides when applicable. For simplicity,  $R'$  and  $S'$  are set to  $R$  and  $S$ , respectively. As shown in [4], the basic distance and velocity resolutions of the OFDM radar read  $\Delta d = c/(2 S \Delta f)$  and  $\Delta v = c/(2 R T_s f_c)$ , respectively, with  $c$  denoting the speed of light, which correspond to the resolution in the range–Doppler map. The resolution values for different waveform configurations are also shown in Table I. No further peak refinement methods are adopted in these simulations. Finally, a basic rectangular window is used as the window function in (5).

In these reference evaluations, only a single target is present, and we vary the true distance and speed of the target randomly, from realization to another, with uniform distributions within 20–200 m (distance) and –40 to 40 m/s (velocity). In the radar processing, no prior information about the target distance or speed is assumed, and thus in the periodogram calculations and the corresponding detector, the overall feasible space  $\Omega_A$  contains distances up of a one-way propagation delay of half the cyclic prefix and velocities

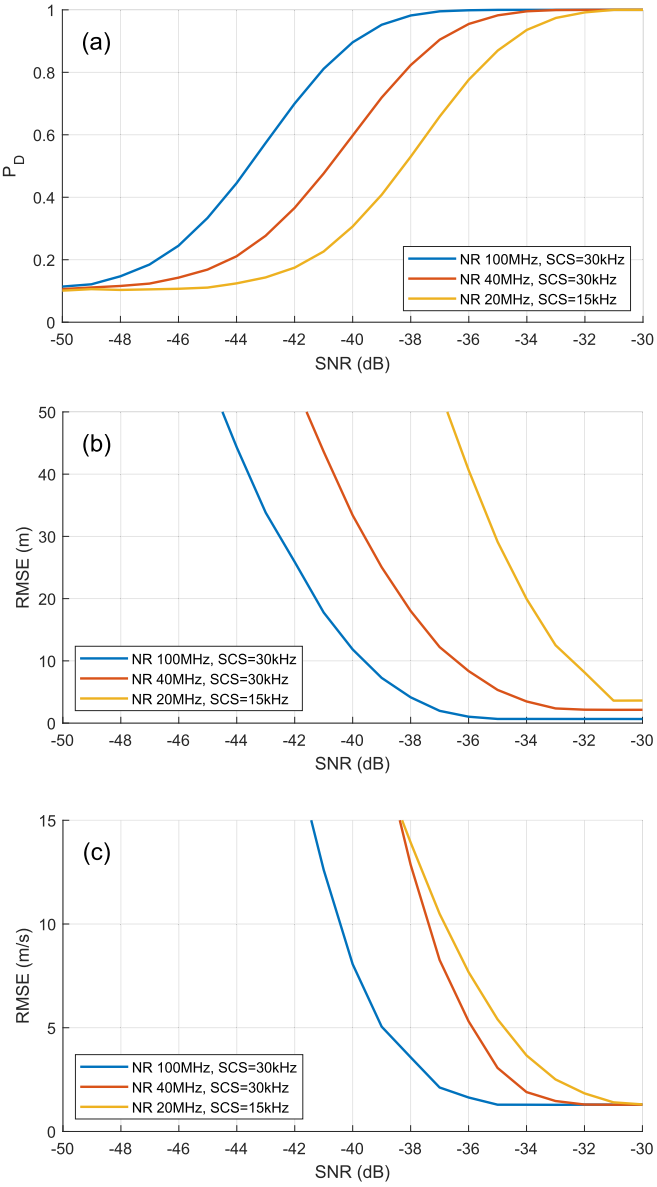


Fig. 2. Single-target radar performance at 3.5 GHz as a function of receiver input SNR, in terms of (a) detection probability ( $P_D$ ), (b) target distance estimation RMSE, and (c) target velocity estimation RMSE, for 10-ms NR waveforms with 20, 40, and 100 MHz carrier bandwidths.

up to a Doppler shift of  $\pm 10\%$  of the subcarrier spacing. The distance limit is directly stemming from the subcarrier-based processing, to avoid intersymbol interference (ISI), while the velocity/Doppler limit is a practical engineering rule of thumb, to keep intercarrier interference (ICI) tolerable [4], [16]. The detection threshold  $T_{\text{th}}$  is set such that  $P_{\text{FA},\text{tot}} = 10\%$ . The numerical values of these limits are also shown in Table I.

We also consider multipath components, i.e., there are indirect reflected and/or scattered waves entering the receiver in addition to the direct reflection. The total power of the reflected and scattered multipath components is  $-15$  dB, relative to the direct reflected component, with an rms delay spread of 100 ns, representing a realistic example scenario.

Fig. 2 shows the obtained probability of target detection for varying receiver input SNR, as well as the corresponding

distance and velocity estimation error behavior—calculated only when the target detection is positive—for the considered NR channel bandwidth and subcarrier spacing cases shown in Table I. LTE 20 MHz is eventually not shown since its performance is essentially identical to NR 20 MHz. As can be observed, reliable target detection can be achieved down to input SNRs in the order of  $-30$  to  $-40$  dB, the exact number depending on the channel bandwidth and the required probability of detection. In general, as discussed in [3] and [6], the subcarrier-based radar processing provides a processing gain of

$$\Gamma_P = 10 \log_{10}(R \times S) \quad (8)$$

decibels against thermal noise, thus with given receiver input SNR, the larger processing gains obtained through larger bandwidths improve the detection, as shown in Fig. 2(a).

In addition, the results in Fig. 2 illustrate that at these SNR values, where high detection probabilities are obtained, also the distance and velocity estimation errors are well-behaving. The results also clearly show that when the probability of detection is approaching 100%, the estimates' RMSE values are essentially directly defined by the resolution values shown in Table I. In other words, the RMSE values are converging toward  $((\Delta d)^2/12)^{1/2}$  and  $((\Delta v)^2/12)^{1/2}$  for distance and velocity, respectively, reflecting uniform error distribution within the pixel width.

Overall, we observe that the large carrier bandwidths available in NR, even at sub-6 GHz frequencies [18], build a basis for good target estimation accuracy and precision, particularly when it comes to the distance estimation. In general, 5G NR networks can also be deployed at 24–40 GHz bands [18], with continuous carrier bandwidths up to 400 MHz available already in 3GPP Release 15, which together with the larger center frequencies facilitate further improvements in both distance and velocity estimation resolutions.

### III. SELF-INTERFERENCE PROBLEM AND CANCELLATION SOLUTIONS

#### A. TX–RX Isolation and Self-Interference Problem

In ordinary TDD-based communication networks, the transmit and receive functionalities are divided in time, and thus a base station's transmitter and receiver do not need to operate simultaneously. However, in both LTE and NR networks, the minimum downlink allocation within a radio frame contains seven OFDM symbols, or one slot, which corresponds to 0.5 ms with 15 kHz subcarrier spacing. Hence, from the point of view of the considered OFDM radar concept, the receiver must be operating simultaneously unlike in a pulsed radar; otherwise, no targets within tens of kilometers could be detected rendering the whole concept useless.

The fact that the receiver must be operating simultaneously while transmitting, and at the same carrier frequency, leads to large implementation challenges, particularly in facilitating sufficient transmitter–receiver isolation [12], [19], [23], [28], [37]–[40]. This calls for new hardware, to replace the TDD RF switching with more elaborate circulator [20], [23]–[25] or EBD [12], [26], [27] type of circuitries, and has

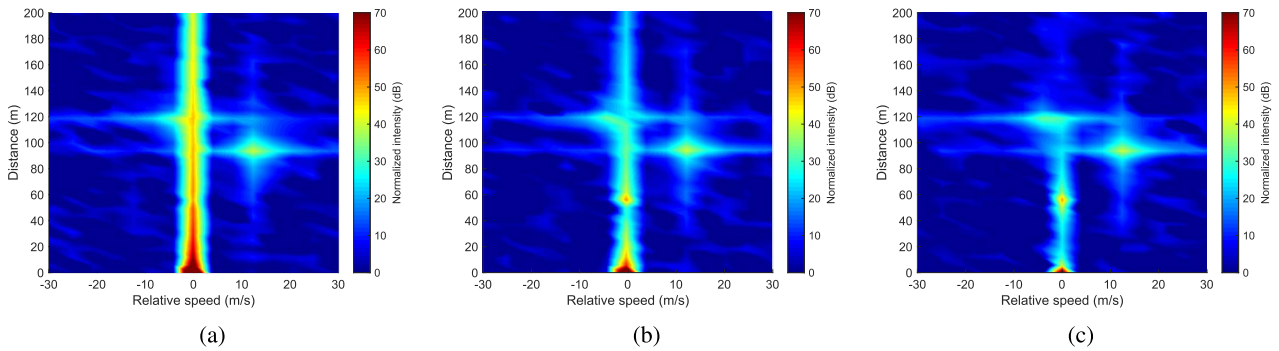


Fig. 3. Example radar images in a scenario with three true targets located at 60, 90, and 120 m distances and moving with relative velocities of 0, +12, and -2 m/s. The radar receiver operates under direct SI levels of (a) 70 dB, (b) 50 dB, and (c) 30 dB with respect to the thermal noise floor. NR waveform of 10 ms with a channel bandwidth of 40 MHz and subcarrier spacing of 30 kHz is used.

been studied actively over the recent years, under the in-band full-duplex radio terminology, with primarily communications applications in mind (see [19], [23], [37]–[45]). In the radar context, the SI stemming from the direct coupling of the transmit signal to the receiver can be interpreted as a strong static target at a very short distance [11], [12], [33], [46]. Hence, one could argue that as long as a certain level of TX–RX isolation can be provided, such that the low noise amplifier (LNA) and the rest of the sensitive receiver electronics can tolerate the remaining SI, the true echoes stemming from true targets can be separated in the radar processing. Recent examples of radar-domain processing solutions for direct interference and clutter suppression can be found in [32] and [34], developed primarily for passive radar applications, reporting commonly some 15–20 dB processing gain at best.

However, since the eNB/gNB transmit power can be even more than 140 dB larger than the receiver thermal noise floor, facilitating sufficient TX–RX isolation as a whole is technically very challenging, particularly in the monostatic shared-antenna OFDM radar case with limited passive isolation and high peak-to-average power ratio (PAPR) in the transmit waveform. An extreme example is a macrobase station that commonly utilizes a transmit power in the order of +46 dBm, while the receiver noise floor assuming 20 MHz channel bandwidth and 4 dB noise figure is only -97 dBm. For one, with such transmit powers and large PAPR, preventing LNA and receiver saturation is already a fundamental problem. In addition, the powerful SI component in the receiver digital signal can largely mask the true echoes and targets—particularly those that are static, but also other slowly moving targets—rendering thus very tough requirements for the digital-domain suppression algorithms.

A concrete example of the latter problem is given in Fig. 3, showing the OFDM radar-based range–velocity profiles, i.e., radar images, when the reflections of three true targets are observed and processed by the receiver, under different levels of the direct SI. In this case, an NR signal with a channel bandwidth of 40 MHz and subcarrier spacing of 30 kHz is used, and a complete 10 ms radio frame is transmitted and processed. The direct SI entering the receiver is either 70, 50, or 30 dB above the receiver thermal noise floor, corresponding to Fig. 3(a)–(c), respectively, and contains only a single coupling path with nanosecond scale delay.

It can be clearly observed that the direct SI is reflected in the radar processing as a strong static target located essentially at zero distance. Furthermore, and importantly, the sidelobes of the SI produce a substantial masking effect, which largely complicates the detection of true weaker targets moving with lower velocities along a wide range of distances, despite the true SI has negligibly small physical coupling delay and zero Doppler.

In general, as shown in (8), the subcarrier-based radar processing presented in Section II provides large processing gain against noise. This, thus, provides a corresponding SNR improvement for detecting weak target reflections way below the thermal noise floor, as demonstrated already along Fig. 2. However, similar to clutter, the direct SI component is also subject to the same processing gain, and therefore, this does not solve the isolation challenge. In addition, as the basic power calculations show above, more than 100 dB of total SI suppression is required, which calls for multiple complementary methods as no single technique can facilitate such high isolation. Hence, we can conclude that on top of basic passive RF isolation and radar-domain digital suppression methods, efficient active RF and digital SI cancellation methods are needed, particularly from the static and slow-moving targets' viewpoint, as well as overall to prevent receiver saturation.

### B. RF and Digital Cancellation Solutions

As identified above, facilitating sufficient TX–RX isolation is a key technical ingredient in OFDM radars. In this work, on top of passive isolation, we primarily focus on active RF cancellation and time-domain digital cancellation methods. Compared to the existing in-band full-duplex radio research, a specific radar-related flavor is that only the direct SI should be canceled or suppressed, along with possible reflections from very close-by surfaces, while the echoes from true targets must be preserved. This is one clear difference to all earlier full-duplex radio works, such as [41], [47], and [48], which do not separate between the direct and reflected SI components. In addition, we note that agnostic digital cancellation techniques, independent of the specific radar processing approach, are pursued, which can then be complemented with, e.g., the CLEAN-like methods [11], [12], [32], [33], operating in the radar domain.

In general, despite a monostatic shared-antenna OFDM radar is pursued, the so-called direct SI can contain frequency selectivity in its coupling response [45], [48]. Hence, a properly devised multitap RF canceller is adopted, seeking to protect the LNA and the following receiver chain. A similar architecture as in our earlier work in [47] is adopted such that the RF canceller uses the power amplifier (PA) output as a reference, tapping it through multiple parallel RF delays and vector modulators to obtain an accurate estimate of the direct SI.

In this work, we consider three RF taps and formally express the signal after the RF canceller as  $y_{RF}(t) = r_{RF}(t) - \hat{s}_{RF}(t)$  where  $r_{RF}(t)$  is denoting the receiver input signal, while the actual RF cancellation signal  $\hat{s}_{RF}(t)$  reads

$$\hat{s}_{RF}(t) = \sum_{l=1}^3 \alpha_l (\cos(\theta_l) x_{RF}^0(t - \tau_l) - \sin(\theta_l) x_{RF}^{90}(t - \tau_l)). \quad (9)$$

In above,  $x_{RF}(t)$  denotes the PA output signal,  $\tau_l$  is the RF delay of the  $l$ th tap,  $\alpha_l$  and  $\theta_l$  refer to the adjustable amplitude and phase values of the  $l$ th vector modulator, and  $x_{RF}^0(t)$  and  $x_{RF}^{90}(t)$  denote the  $0^\circ$  and  $90^\circ$  phase-shifted tap signals inside a vector modulator, respectively. In the RF canceller design, we set the maximum delay  $\tau_3$  to 10 ns, which corresponds to round 3 m equivalent distance. This way, we can still facilitate modeling frequency selectivity in the direct SI coupling channel, while essentially avoid canceling any echoes from true targets that are located more than 1.5 m away.

To accurately reduce the direct SI component power at the RF canceller output, proper real-time control of the amplitude and phases value,  $\alpha_l$  and  $\theta_l$ ,  $l = 1, 2, 3$ , is essential. We have implemented a digital control system where complex I/Q downconverted observations of the tapped PA outputs and the RF canceller output, denoted by  $x_{RF}^{IQ}(t)$  and  $y_{RF}^{IQ}(t)$ , respectively, are utilized. Building on gradient-based learning [47], implemented digitally on an field-programmable gate array (FPGA), and combining the amplitudes and phases into corresponding complex coefficients  $c_l = \alpha_l e^{j\theta_l}$  inside the digital control system, the RF canceller parameter learning can be expressed as

$$c_l \leftarrow c_l + \mu_{RF} \int [x_{RF}^{IQ}(t - \tau_l)]^* y_{RF}^{IQ}(t) dt \quad (10)$$

where  $\mu_{RF}$  is the learning step size,  $[\cdot]^*$  refers to complex conjugation, and the integration is performed digitally through the corresponding sampled I/Q signals. The digital control and tracking of the RF canceller weights are shown by measurements, in Section IV, to provide more than 50 dB of active RF cancellation gain with an example instantaneous bandwidth of 40 MHz. A block diagram illustrating the overall RF canceller entity and its digital control system is shown in Fig. 4(a).

In addition, the residual direct SI after the RF canceller can and must be further suppressed toward the receiver noise floor by using a digital cancellation stage. Inspired by our earlier work in [41] and [49], we adopt a nonlinear digital canceller such that potential TX/RX RF nonlinearities can also be

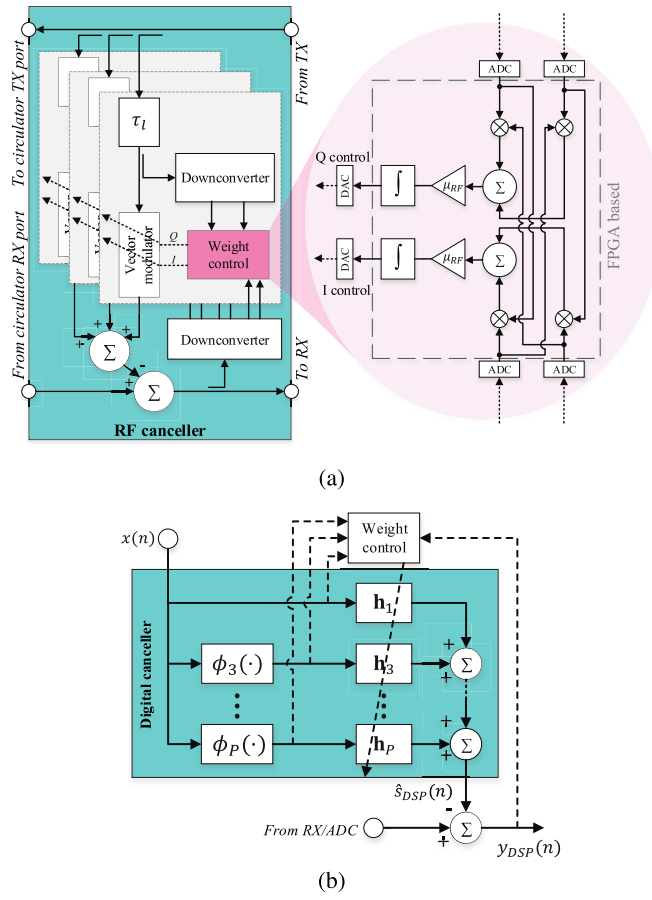


Fig. 4. (a) RF canceller block diagram and self-adaptive weight control. (b) General illustration of the nonlinear digital canceller.

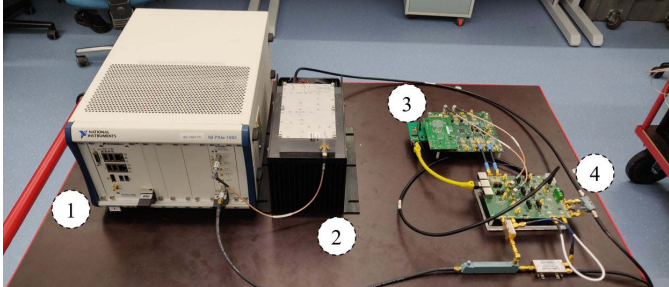
suppressed. Assuming a memory polynomial-based nonlinear processing approach, the corresponding digital cancellation signal can be expressed as

$$\hat{s}_{DSP}(n) = \sum_{p=1}^P \sum_{k=-M_1}^{M_2} h_{p,k} \phi_p(x(n-k)) \quad (11)$$

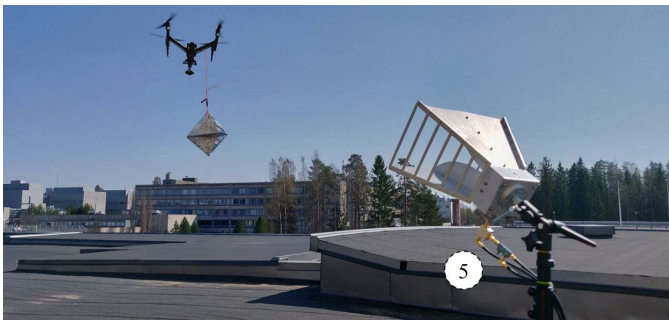
where  $x(n)$  denotes the digital I/Q transmit samples,  $\phi_p(x(n)) = |x(n)|^{p-1} x(n)$ ,  $p = 1, 3, \dots, P$ , are the nonlinear basis functions up to order  $P$ , and  $h_{p,k}$  denote the adjustable filter parameters with  $M_1$  and  $M_2$  precursor and postcursor memory taps, respectively, per each nonlinearity order  $p$ . For parameter estimation, block least-squares (LS) or adaptive filtering methods such as least-mean-square (LMS) or recursive LS (RLS) can, in general, be adopted [39], [41], seeking to minimize the canceled signal power.

As acknowledged already in prior literature [39], [41], different nonlinear basis functions  $\phi_p(x(n))$ ,  $p = 1, 3, \dots, P$ , are largely correlated, which, in turn, complicate parameter estimation, particularly when gradient-based methods are adopted. Instead of explicitly orthogonalizing the basis functions, as done in prior work [39], [41], we adopt a novel self-orthogonalizing learning rule in this work, expressed as

$$\mathbf{h} \leftarrow \mathbf{h} + \mu_{DSP} \mathbf{C}^{-1} \mathbf{u}(n) y_{DSP}(n) \quad (12)$$



(a)



(b)

Fig. 5. (a) Main equipment used in the RF measurements is shown, namely, ① VST, ② external PA, ③ the developed RF canceller, and ④ its digital control board. (b) Directive TX/RX horn antenna and circulator ⑤ are shown, together with a drone (DJI Inspire-2) carrying a retroreflector.

where  $\mathbf{h}$  is a column-vector collecting the canceller coefficients  $h_{p,k}$ ,  $\forall p, k$ ,  $\mu_{\text{DSP}}$  refers to the learning step-size, and  $\mathbf{C}$  denotes the correlation matrix of the basis function samples, which can be precomputed. In addition,  $\mathbf{u}(n)$  refers to the basis function samples used to calculate the cancellation signal sample  $\hat{s}_{\text{DSP}}(n)$  as shown in (11), while  $y_{\text{DSP}}(n)$  denotes the corresponding sample at the digital canceller output. This approach greatly reduces the computational complexity of the main digital cancellation path, as the explicit basis function orthogonalization utilized in [39] and [41] is avoided. A principal illustration of the digital cancellation system is shown in Fig. 4(b).

Similar to the RF canceller, the memory length of the digital cancellation processing must be chosen with care, in order to avoid suppressing the reflections from true targets. In particular, the amount of the postcursor taps  $M_2$  used in the digital canceller is directly related to the detectable radar range. In our implementation, the digital canceller runs at a sample rate of 240 MHz and contains  $M_1 = 5$  precursor and  $M_2 = 5$  postcursor taps. These correspond to the minimum detectable distance of ca. 3 m for true targets, which is well inline with the RF canceller parameterization.

#### IV. IMPLEMENTATION AND MEASUREMENT RESULTS

##### A. Measurement Setup

The basic elements of the measurement setup are illustrated in Fig. 5, building on the National Instruments PXIe-1082 vector signal transceiver (VST) implementing the basic RF transmitter and receiver functionalities. An external PA with a gain of 42 dB is also utilized, and all the measurements

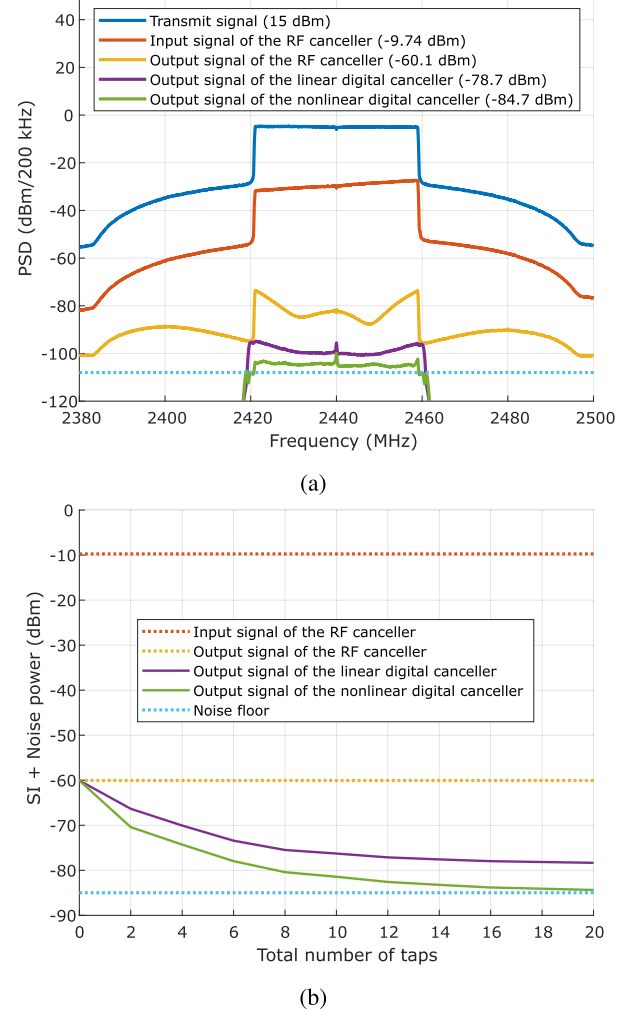


Fig. 6. Overall measured TX-RX isolation performance with 40 MHz NR waveform at 2.44 GHz for (a) five precursor and five postcursor taps and (b) varying a total number of taps in digital cancellation. The order of the nonlinear digital canceller is  $P = 11$ , while the linear digital canceller corresponds to  $P = 1$ .

are carried out at the 2.4 GHz ISM band with ca. +20 dBm transmit power. The RF canceller and its digital control functionalities are implemented on separate boards, properly interfaced to the VST and the external PA. A directive LB-880 horn antenna with 10 dBi of antenna gain is adopted and shared between the TX and RX through a circulator (JQL JCC2300T2500S6), which together provide some 25 dB of passive TX–RX isolation, partially due to antenna reflection and partially due to finite isolation between the circulator TX and RX ports. The digital SI cancellation and radar processing are implemented in the VST host processing environment.

In all the measurements, a 5G NR waveform with a sub-carrier spacing of 30 kHz and 40 MHz channel bandwidth is adopted (cf. Table I), with FFT/IFFT size of 2048 implying a core I/Q time-domain sample rate of  $2048 \times 30 \text{ kHz} = 61.44 \text{ MHz}$ . Further PAPR reduction and OFDM symbol windowing are also implemented in the transmitter chain. The digital front-end sample rate is 240 MHz at which the digital SI canceller is also running. The order of the digital canceller is either  $P = 1$  (linear digital canceller) or  $P = 11$  (nonlinear digital canceller). After the digital cancellation, the digital

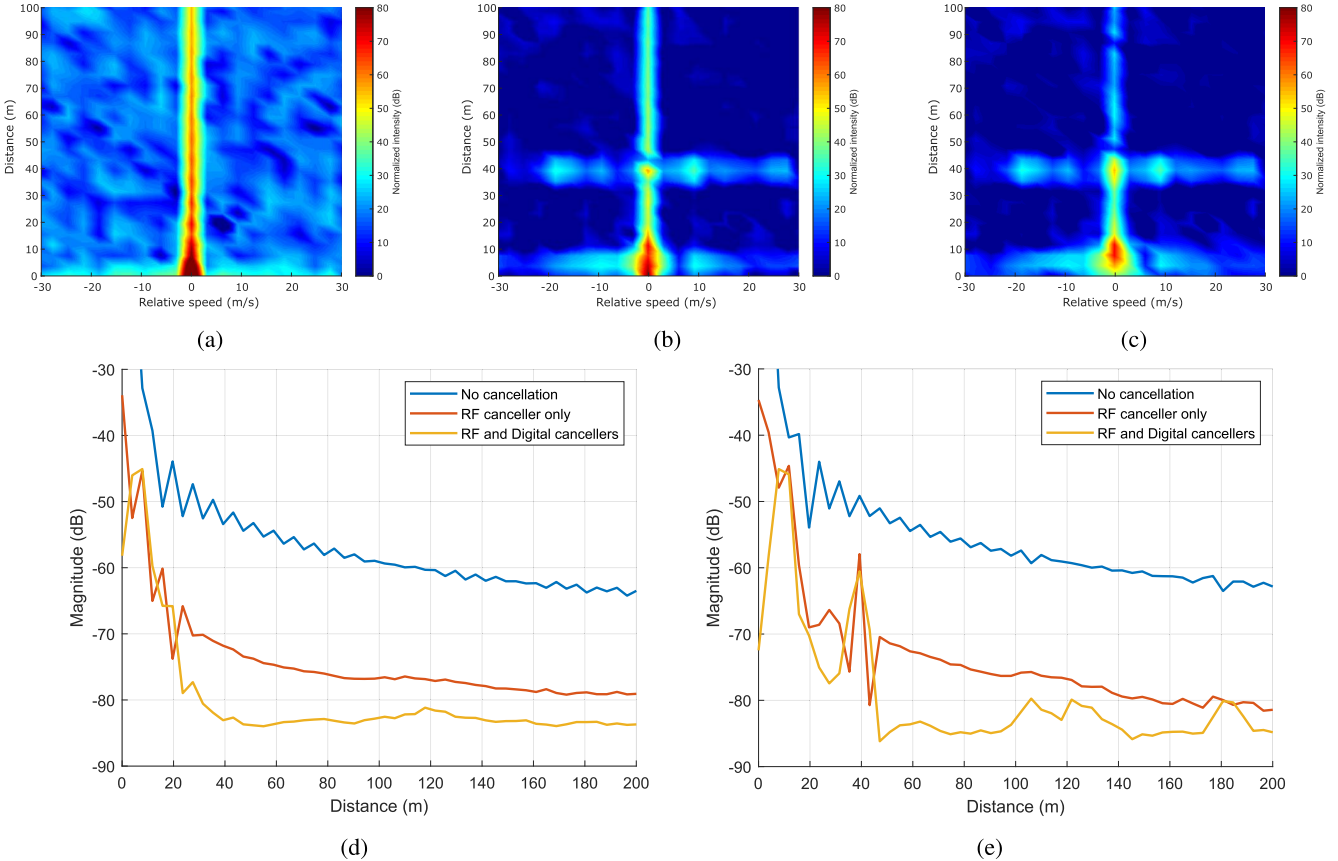


Fig. 7. Measured radar images with a static airborne drone at a distance of 40 m (a) without any cancellation, (b) with RF cancellation only, and (c) with both RF and digital cancellation. (d) and (e) Distance estimation profiles of reference measurement (no target) and drone measurement are shown, respectively, illustrating also the additional leakage suppression gain from the RF and digital cancellers.

received signal is downsampled by 125/32 to the fundamental I/Q sample rate of 61.44 MHz. In addition, the Hamming window [28] is used in the periodogram calculations in all the measurements.

### B. Measured TX–RX Isolation

Before going to the actual radar experiments, the achievable total TX–RX isolation of the developed demonstrator system incorporating the RF and digital cancellation solutions is measured and illustrated. An example of the power spectral densities in different stages of the transceiver system is shown in Fig. 6(a), measured in an anechoic chamber with an antenna connected, while no actual targets are present. We can observe that the RF canceller provides more than 50 dB of the direct SI suppression, while being then further complemented by the digital canceller such that an overall isolation of ca. 100 dB is reached. We also note that the total isolation provided by the circulator and the active RF canceller is some 75 dB, which is very essential to prevent receiver saturation, especially with larger transmit powers. Such 75 dB RF isolation is already close to the isolation provided by high-quality base-station duplex filters in frequency-division duplexing (FDD)-based networks [16], hence potentially facilitating simultaneous transmission and reception for transmit powers up to +40 dBm, or even +46 dBm, from the receiver linearity and saturation point of view.

The figure also clearly shows that the linear digital canceller is limited by the RF nonlinearities, while the nonlinear digital canceller can also efficiently suppress the nonlinear leakage. This is one complementary ingredient that the radar domain-based direct leakage cancellers cannot most likely facilitate. To better assess the impact of the digital canceller parameterization, in terms of the number of precursor and postcursor taps, Fig. 6(b) shows the integrated passband powers for varying numbers of total taps in the digital canceller while also comparing the linear and nonlinear digital cancellers. We can conclude that increasing the amount of the canceller taps, and hence complexity, beyond the case of 5+5 provides only a marginal performance improvement. Hence, in all the following experiments, the 5+5 configuration is adopted.

### C. Sensing Static Targets Under SI

Next, we continue with the RF measurements through actual outdoor experiments containing real targets. As a first example, we utilize a commercial drone flying at around 38 m height above the OFDM radar system holding a multi-faceted reflector as illustrated already in Fig. 5(b). The drone is deliberately staying at fixed coordinates, thus representing a static airborne target at an overall distance of some 40 m. Fig. 7(a) shows the corresponding measured radar image, yet without any RF or digital cancellation, meaning that only the passive circulator isolation is utilized. It can clearly be

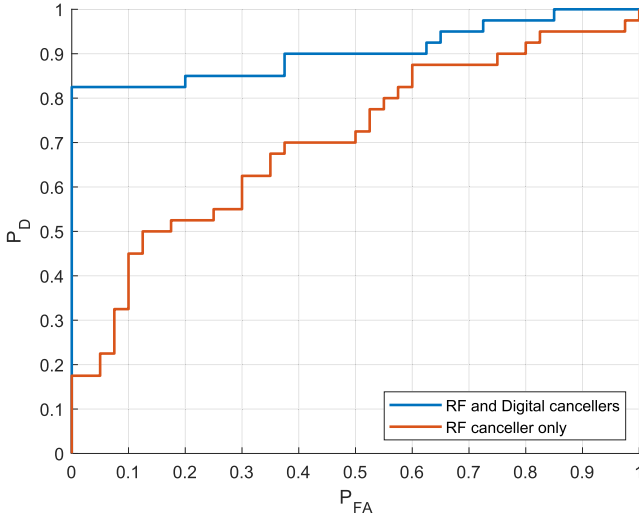


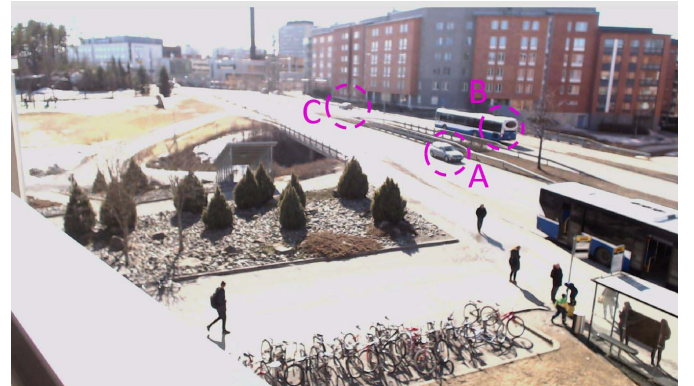
Fig. 8. Measured ROC curves in the drone scenario, with RF canceller only and with both RF and digital cancellers.

observed, similar to the synthetic data-based radar images in Fig. 3, that the SI corresponds to a very strong static target located essentially at zero distance and zero velocity and also that the sidelobes are strong up to large distances.

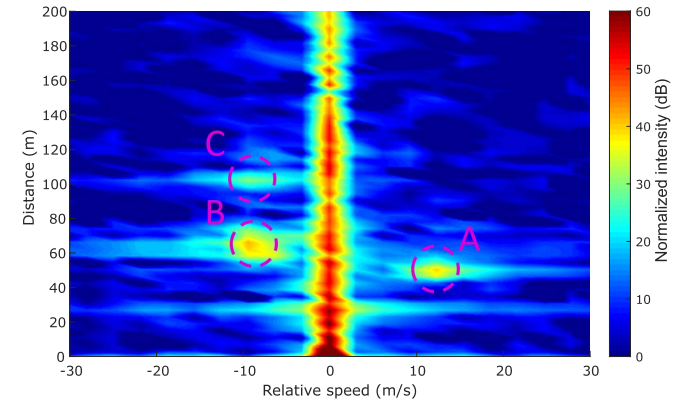
Then, Fig. 7(b) and (c) shows how the OFDM radar-based range–Doppler maps are improving when the presented RF canceller, in (b), or both the RF and digital cancellers, in (c), are also applied. Opposed to Fig. 7(a), a clear static target is now seen at around the distance corresponding to the drone. It is also noted that even though the drone is remaining at a fixed distance with zero velocity during the measurements, the radar image shows some additional peaks at the same distance of 40 m, but nonzero velocity. These are stemming from the propellers’ rotation, i.e., reflect the micro-Doppler phenomenon. Overall, the measurement-based observations are well inline with the simulated results discussed along Fig. 3.

To further assess and visualize the impact of the cancellers, we carry out additional reference measurements such that the antennas are tilted toward the sky and no actual targets are present. This way, the receiver is essentially observing and processing only the SI and some residual reflections and clutter from the surroundings. The range profile of such reference measurements is shown in Fig. 7(d), while the corresponding range profile of the drone measurements is shown in Fig. 7(e). By comparing the range profiles, we can clearly observe that there is a relatively strong reflection at a distance of ca. 10 m, caused most likely by the antenna sidelobe and close-by building surface. In addition, the figures clearly illustrate the improved dynamic range offered by the RF and digital cancellers. When both the RF and digital cancellers are adopted, also reflections from high-rise buildings at distances of some 120 and 180 m can be observed, reflecting the increased dynamic range.

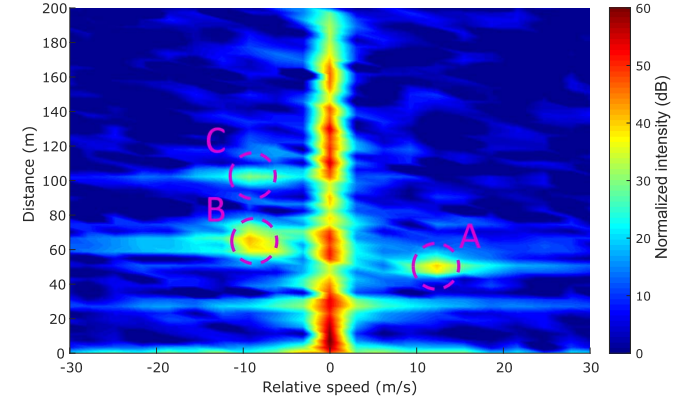
Next, we assess the impact of the RF and digital cancellers on the actual drone detection, through the measured data. We first measure 100 radar images without the drone (hypothesis  $H_0$ ) and another 100 radar images with the drone (hypothesis  $H_1$ ). Then, we calculate the empirical distributions of the radar images for both data sets, covering



(a)



(b)



(c)

Fig. 9. (a) Vehicular measurement scenario with three moving cars A, B, and C located at snapshot distances of 51.1, 66.8, and 102.1 m, respectively, driving along the road such that the velocity relative to the radar system is ca. 12, -9, and -9 m/s, respectively. The corresponding measured radar images with (b) RF canceller only and (c) both RF and digital cancellers, using an NR waveform of 20 ms with a channel bandwidth of 40 MHz and subcarrier spacing of 30 kHz, are shown.<sup>1</sup>

3 × 3 pixels of the periodograms at and around the drone location. We then vary the detection threshold  $T_{\text{th}}$  and evaluate the probability of detection and probability of false alarm through the measured empirical distributions. These compose the measured receiver operating characteristics (ROCs) curve, shown visually in Fig. 8. The improvement provided by the

<sup>1</sup>Supplemental material for the reader can be downloaded online at <http://ieeexplore.ieee.org/>

digital canceller, compared to RF canceller only, can be clearly observed.

#### D. Sensing Moving Targets Under SI

The overall OFDM radar system concept comprising the canceller solutions is next demonstrated and evaluated in a typical vehicular traffic scenario with three moving cars. Fig. 9(a) illustrates the measurement scenario where three vehicles labeled *A*, *B*, and *C* are driving along a road toward the OFDM radar system at distances of some 50–110 m. The measurement equipment and the antenna are located in the third floor of one of the university buildings, located next to a road with 50 km/h speed limit, and the circulator-based shared antenna system is again adopted.

The corresponding measured radar images shown in Fig. 9(b) with RF cancellation only and in Fig. 9(c) with both RF and digital cancellers demonstrate that the proposed system is clearly able to sense all three moving vehicles despite the strong reflections coming from the surrounding buildings as well as the static clutter. The estimated snap-shot distances and velocities of the vehicles *A*, *B*, and *C*, building on one radar image calculated over two NR radio frames, i.e., 20 ms, are 51.1, 66.8, and 102.1 m, with relative speeds of 12, −9, and −9 m/s, respectively. As the radar transmit-receive system and the corresponding antenna unit are not placed in the main road direction, the estimated velocities correspond to the velocity projection along a line between the considered vehicle and the radar system. Estimating that the angle between the main vehicle trajectory and the radar system location is ca. 20°, the absolute velocities of the three vehicles are between 30 and 40 km/h, which are consistent with the speed limit of the road.

Additional multimedia content is available to the reader online.<sup>1</sup> In this multimedia illustration, a video recording of the moving cars is shown, together with displaying a sequence of the corresponding radar images, side by side. Each radar image is calculated over one 20 ms NR radio frame, while the overall experiment corresponds to ca. 10 s of real time. The sequence of the radar images is illustrating that moving vehicles can be efficiently sensed, despite the static reflections and ground clutter.

## V. CONCLUSION

In this article, the use of the LTE and 5G NR downlink waveforms for radar/sensing purposes was addressed and studied, together with the fundamental hardware challenges related to transmitter-receiver (TX-RX) isolation and associated SI problem. First, frequency-domain radar processing building on the LTE or NR time-frequency resource grid, complemented with interpolation to account for missing samples due to the null subcarriers within the transmit waveform passband, was described. Assuming ideal TX-RX isolation, for reference, the achievable target detection as well as the corresponding range and velocity estimation performances of the considered method were then evaluated numerically. In particularly, the large channel bandwidths supported by 5G NR were shown to provide good sensing

performance already at below 6 GHz frequencies. With 100 MHz channel bandwidth, distance estimation accuracy in the order of 1 m and target detection probability exceeding 90% were shown to be feasible at SNRs lower than −30 dB.

Then, the fundamental TX-RX isolation challenge was addressed, with specific emphasis on monostatic shared-antenna base-station deployments. To prevent receiver saturation and to reduce the inherent masking effect of the direct leakage sidelobes, efficient RF and digital cancellation solutions were described, properly tailored to the OFDM radar use case such that frequency-selective TX-RX coupling can be handled while the actual reflections from true targets are preserved. Comprehensive RF measurements were provided, verifying the basic hypothesis, as well as concretely showcasing successful sensing of static and moving targets, such as drones and cars, while evidencing measured TX-RX isolation of approximately 100 dB. Our future work will focus on extending the 5G NR-based radio sensing research toward the mmWave bands, particularly 28 and 39 GHz that are already standardized for NR. In addition, we study the potential and feasibility of simultaneously receiving an in-band uplink data signal while still sensing the reflections of the downlink transmit signal, all at the same channel.

## REFERENCES

- [1] B. Paul, A. R. Chiriyath, and D. W. Bliss, "Survey of RF communications and sensing convergence research," *IEEE Access*, vol. 5, pp. 252–270, 2017.
- [2] L. Han and K. Wu, "Joint wireless communication and radar sensing systems—State of the art and future prospects," *IET Microw. Antennas Propag.*, vol. 7, no. 11, pp. 876–885, Aug. 2013.
- [3] C. Sturm and W. Wiesbeck, "Waveform design and signal processing aspects for fusion of wireless communications and radar sensing," *Proc. IEEE*, vol. 99, no. 7, pp. 1236–1259, Jul. 2011.
- [4] K. M. Braun, "OFDM radar algorithms in mobile communication networks," Ph.D. dissertation, Karlsruhe Inst. Technol., Karlsruhe, Germany, 2014.
- [5] Y. L. Sit, C. Sturm, and T. Zwick, "Doppler estimation in an OFDM joint radar and communication system," in *Proc. IEEE German Microw. Conf.*, Mar. 2011, pp. 1–4.
- [6] C. Sturm, T. Zwick, and W. Wiesbeck, "An OFDM system concept for joint radar and communications operations," in *Proc. IEEE 69th Veh. Technol. Conf.*, Apr. 2009, pp. 1–5.
- [7] B. Schweizer, C. Knill, D. Schindler, and C. Waldschmidt, "Stepped-carrier OFDM-radar processing scheme to retrieve high-resolution range-velocity profile at low sampling rate," *IEEE Trans. Microw. Theory Techn.*, vol. 66, no. 3, pp. 1610–1618, Mar. 2018.
- [8] C. Knill, B. Schweizer, S. Sparre, F. Roos, R. F. H. Fischer, and C. Waldschmidt, "High range and Doppler resolution by application of compressed sensing using low baseband bandwidth OFDM radar," *IEEE Trans. Microw. Theory Techn.*, vol. 66, no. 7, pp. 3535–3546, Jul. 2018.
- [9] A. Evers and J. A. Jackson, "Analysis of an LTE waveform for radar applications," in *Proc. IEEE Radar Conf.*, May 2014, pp. 0200–0205.
- [10] C. B. Barneto, L. Anttila, M. Fleischer, and M. Valkama, "OFDM radar with LTE waveform: Processing and performance," in *Proc. IEEE Radio Wireless Symp. (RWS)*, Jan. 2019, pp. 1–4.
- [11] Y. Zeng, Y. Ma, and S. Sun, "Joint radar-communication: Low complexity algorithm and self-interference cancellation," in *Proc. IEEE Global Commun. Conf. (GLOBECOM)*, Dec. 2018, pp. 1–7.
- [12] S. A. Hassani, A. Guevara, K. Parashar, A. Bourdoux, B. van Liempd, and S. Pollin, "An in-band full-duplex transceiver for simultaneous communication and environmental sensing," in *Proc. Asilomar Conf. Signals, Syst., Comput. (ASILOMAR)*, Oct. 2018, pp. 1389–1394.
- [13] R. Blázquez-García, J. Casamayón-Antón, and M. Burgos-García, "LTE-R based passive multistatic radar for high-speed railway network surveillance," in *Proc. Eur. Radar Conf.*, Sep. 2018, pp. 6–9.
- [14] Y. Dan, X. Wan, J. Yi, and Y. Rao, "Ambiguity function analysis of long term evolution transmission for passive radar," in *Proc. Int. Symp. Antennas, Propag., EM Theory (ISAPE)*, Dec. 2018, pp. 1–4.

- [15] Y. Wang, T. Phelps, K. Kibaroglu, M. Sayiner, Q. Ma, and G. M. Rebeiz, "28 GHz 5G-based phased-arrays for UAV detection and automotive traffic-monitoring radars," in *IEEE MTT-S Int. Microw. Symp. Dig.*, Philadelphia, PA, USA, Jun. 2018, pp. 895–898.
- [16] E. Dahlman, S. Parkvall, and J. Sköld, *5G NR: The Next Generation Wireless Access Technology*. New York, NY, USA: Academic, 2018.
- [17] *Evolved Universal Terrestrial Radio Access (E-UTRA); Base Station (BS) Radio Transmission and Reception Release 15*, document TS 36.104 v15.3.0, Technical Specifications Group Radio Access Network, 3GPP, Jun. 2018.
- [18] *NR; Base Station (BS) Radio Transmission and Reception Release 15*, document TS 38.104 v15.4.0, Technical Specifications Group Radio Access Network, 3GPP, Dec. 2018.
- [19] K. E. Kolodziej, B. T. Perry, and J. S. Herd, "In-band full-duplex technology: Techniques and systems survey," *IEEE Trans. Microw. Theory Techn.*, vol. 67, no. 7, pp. 3025–3041, Jul. 2019.
- [20] M. Biedka, Y. E. Wang, Q. M. Xu, and Y. Li, "Full-duplex RF front ends : From antennas and circulators to leakage cancellation," *IEEE Microw. Mag.*, vol. 20, no. 2, pp. 44–55, Feb. 2019.
- [21] A. Sabharwal, P. Schniter, D. Guo, D. W. Bliss, S. Rangarajan, and R. Wichman, "In-band full-duplex wireless: Challenges and opportunities," *IEEE J. Sel. Areas Commun.*, vol. 32, no. 9, pp. 1637–1652, Sep. 2014.
- [22] E. Everett, A. Sahai, and A. Sabharwal, "Passive self-interference suppression for full-duplex infrastructure nodes," *IEEE Trans. Wireless Commun.*, vol. 13, no. 2, pp. 680–694, Jan. 2014.
- [23] S. Khaledian, F. Farzami, B. Smida, and D. Erricolo, "Inherent self-interference cancellation for in-band full-duplex single-antenna systems," *IEEE Trans. Microw. Theory Techn.*, vol. 66, no. 6, pp. 2842–2850, Jun. 2018.
- [24] A. Nagulu and H. Krishnaswamy, "Non-magnetic 60 GHz SOI CMOS circulator based on loss/dispersion-engineered switched bandpass filters," in *Proc. IEEE Int. Solid-State Circuits Conf. (ISSCC)*, Feb. 2019, pp. 446–448.
- [25] T. Dinc and H. Krishnaswamy, "A 28 GHz magnetic-free non-reciprocal passive CMOS circulator based on spatio-temporal conductance modulation," in *Proc. IEEE Int. Solid-State Circuits Conf. (ISSCC)*, Feb. 2017, pp. 294–295.
- [26] Y. S. Choi, C. S. Cho, and Y.-J. Kim, "Improved Tx-to-Rx isolation of radar transceivers using integrated full duplexer with PLL," in *Proc. IEEE Int. Conf. Radar (RADAR)*, Aug. 2018, pp. 1–4.
- [27] B. van Liempd, A. Visweswaran, S. Ariumi, S. Hitomi, P. Wambacq, and J. Craninckx, "Adaptive RF front-ends using electrical-balance duplexers and tuned saw resonators," *IEEE Trans. Microw. Theory Techn.*, vol. 65, no. 11, pp. 4621–4628, Nov. 2017.
- [28] M. A. Richards, W. A. Holm, and J. A. Scheer, *Principles of Modern Radar: Basic Principles*. London, U.K.: IET, 2010.
- [29] A. G. Stove, "Linear FMCW radar techniques," *Proc. Inst. Elect. Eng.—Radar Signal Process.*, vol. 139, no. 5, pt. F, pp. 343–350, Oct. 1992.
- [30] A. Melzer, A. Onic, F. Starzer, and M. Huemer, "Short-range leakage cancellation in FMCW radar transceivers using an artificial on-chip target," *IEEE J. Sel. Topics Signal Process.*, vol. 9, no. 8, pp. 1650–1660, Dec. 2015.
- [31] G. Wang, J.-M. Muñoz-Ferreras, C. Gu, C. Li, and R. Gómez-García, "Application of linear-frequency-modulated continuous-wave (LFMCW) radars for tracking of vital signs," *IEEE Trans. Microw. Theory Techn.*, vol. 62, no. 6, pp. 1387–1399, Jun. 2014.
- [32] K. Chetty, G. E. Smith, and K. Woodbridge, "Through-the-wall sensing of personnel using passive bistatic WiFi radar at standoff distances," *IEEE Trans. Geosci. Remote Sens.*, vol. 50, no. 4, pp. 1218–1226, Apr. 2012.
- [33] S. Mercier, D. Roque, and S. Bidon, "Successive self-interference cancellation in a low-complexity WCP-OFDM radar receiver," in *Proc. Asilomar Conf. Signals, Syst., Comput. (ASILOMAR)*, Oct. 2018, pp. 712–716.
- [34] Y. Liu, J. Yi, X. Wan, X. Zhang, and H. Ke, "Evaluation of clutter suppression in CP-OFDM-based passive radar," *IEEE Sensors J.*, vol. 19, no. 14, pp. 5572–5586, Jul. 2019.
- [35] N. Levanon and E. Mozeson, *Radar Signals*. Hoboken, NJ, USA: Wiley, 2004.
- [36] M. Braun, C. Sturm, and F. K. Jondral, "Maximum likelihood speed and distance estimation for OFDM radar," in *Proc. IEEE Radar Conf.*, May 2010, pp. 256–261.
- [37] D. Bharadia, E. McMilin, and S. Katti, "Full duplex radios," *ACM SIGCOMM Comput. Commun. Rev.*, vol. 43, no. 4, pp. 375–386, Sep. 2013.
- [38] B. Debaillie *et al.*, "Analog/RF solutions enabling compact full-duplex radios," *IEEE J. Sel. Areas Commun.*, vol. 32, no. 9, pp. 1662–1673, Sep. 2014.
- [39] D. Korpi *et al.*, "Full-duplex mobile device: Pushing the limits," *IEEE Commun. Mag.*, vol. 54, no. 9, pp. 80–87, Sep. 2016.
- [40] Y. Liu, P. Roblin, X. Quan, W. Pan, S. Shao, and Y. Tang, "A full-duplex transceiver with two-stage analog cancellations for multipath self-interference," *IEEE Trans. Microw. Theory Techn.*, vol. 65, no. 12, pp. 5263–5273, Dec. 2017.
- [41] D. Korpi, M. Heino, C. Icheln, K. Haneda, and M. Valkama, "Compact inband full-duplex relays with beyond 100 dB self-interference suppression: Enabling techniques and field measurements," *IEEE Trans. Antennas Propag.*, vol. 65, no. 2, pp. 960–965, Feb. 2017.
- [42] T. Riihonen, S. Werner, and R. Wichman, "Mitigation of loopback self-interference in full-duplex MIMO relays," *IEEE Trans. Signal Process.*, vol. 59, no. 12, pp. 5983–5993, Dec. 2011.
- [43] Z. Zhang, X. Chai, K. Long, A. V. Vasilakos, and L. Hanzo, "Full duplex techniques for 5G networks: Self-interference cancellation, protocol design, and relay selection," *IEEE Commun. Mag.*, vol. 53, no. 5, pp. 128–137, May 2015.
- [44] S. Hong *et al.*, "Applications of self-interference cancellation in 5G and beyond," *IEEE Commun. Mag.*, vol. 52, no. 2, pp. 114–121, Feb. 2014.
- [45] M. Heino *et al.*, "Recent advances in antenna design and interference cancellation algorithms for in-band full duplex relays," *IEEE Commun. Mag.*, vol. 53, no. 5, pp. 91–101, May 2015.
- [46] S. Mercier, D. Roque, and S. Bidon, "Study of the target self-interference in a low-complexity OFDM-based radar receiver," *IEEE Trans. Aerosp. Electron. Syst.*, vol. 55, no. 3, pp. 1200–1212, Jun. 2019.
- [47] T. Huusari, Y.-S. Choi, P. Liikkanen, D. Korpi, S. Talwar, and M. Valkama, "Wideband self-adaptive RF cancellation circuit for full-duplex radio: Operating principle and measurements," in *Proc. IEEE 81st Veh. Technol. Conf. (VTC Spring)*, May 2015, pp. 1–7.
- [48] M. Duarte, C. Dick, and A. Sabharwal, "Experiment-driven characterization of full-duplex wireless systems," *IEEE Trans. Wireless Commun.*, vol. 11, no. 12, pp. 4296–4307, Dec. 2012.
- [49] L. Anttila, D. Korpi, V. Syrjälä, and M. Valkama, "Cancellation of power amplifier induced nonlinear self-interference in full-duplex transceivers," in *Proc. Asilomar Conf. Signals, Syst., Comput. (ASILOMAR)*, Nov. 2013, pp. 1193–1198.



**Carlos Baquero Barneto** (S'18) received the bachelor's and M.Sc. degrees in telecommunication engineering from the Universidad Politecnica de Madrid (UPM), Madrid, Spain, in 2017 and 2018, respectively. He is currently pursuing the Ph.D. degree at the Department of Electrical Engineering, Tampere University, Tampere, Finland.

His current research interests include waveform sharing for radar and communications.



**Taneli Riihonen** (S'06–M'14) received the D.Sc. degree (Hons.) in electrical engineering from Aalto University, Helsinki, Finland, in August 2014.

From September 2005 to December 2017, he held various research positions at the School of Electrical Engineering, Aalto University. From November 2014 to December 2015, he was a Visiting Associate Research Scientist and an Adjunct Assistant Professor with Columbia University, New York, NY, USA. He is currently an Assistant Professor (tenure track) with the Faculty of Information Technology and Communication Sciences, Tampere University, Tampere, Finland. His current research interests include physical-layer OFDM(A), multiantennas, and relaying and full-duplex wireless techniques, especially the evolution of beyond 5G systems.

Dr. Riihonen was a recipient of the Finnish Technical Sector's Award for the best doctoral dissertation of the year in Finland within all engineering sciences and the EURASIP Best Ph.D. Thesis Award 2017. He has been nominated 11 times as an Exemplary/Top Reviewer of various IEEE journals. He served as an Editor for IEEE COMMUNICATIONS LETTERS from October 2014 to January 2019. He has been serving as an Editor for IEEE WIRELESS COMMUNICATIONS LETTERS since May 2017.



**Matias Turunen** is currently pursuing the M.Sc. degree in electrical engineering at Tampere University (TAU), Tampere, Finland.

He is currently a Research Assistant with the Department of Electrical Engineering, TAU. His current research interests include in-band full-duplex radios with an emphasis on analog RF cancellation, OFDM radar, and 5G New Radio systems.



**Kari Stadius** (S'95–M'03) received the M.Sc., Lic.Tech., and D.Sc. degrees in electrical engineering from the Helsinki University of Technology, Espoo, Finland, in 1994, 1997, and 2010, respectively.

He is currently a Staff Scientist with the Department of Electronics and Nanoengineering, School of Electrical Engineering, Aalto University, Espoo, Finland. He has authored or coauthored more than 100 refereed journal and conference articles in the areas of analog and RF circuit design. His current research interests include the design and analysis of RF transceiver blocks with a special emphasis on frequency synthesis.



**Lauri Anttila** (S'06–M'11) received the M.Sc. and D.Sc. (Hons.) degrees in electrical engineering from the Tampere University of Technology (TUT), Tampere, Finland, in 2004 and 2011, respectively.

From 2016 to 2017, he was a Visiting Research Fellow with the Department of Electronics and Nanoengineering, Aalto University, Helsinki, Finland. Since 2016, he has been a University Researcher with the Department of Electrical Engineering, Tampere University (formerly TUT). He has coauthored more than 100 refereed articles and 3 book chapters. His current research interests include radio communications and signal processing, with a focus on the radio implementation challenges in systems such as 5G, full-duplex radio, and large-scale antenna systems.



**Jussi Rynnänen** (S'99–M'04–SM'16) was born in Ilmajoki, Finland, in 1973. He received the M.Sc. and D.Sc. degrees in electrical engineering from the Helsinki University of Technology, Espoo, Finland, in 1998 and 2004, respectively.

In 2016, he was appointed as the Head of the Department of Electronics and Nanoengineering, Aalto University, Espoo, where he is currently a Professor. He has authored or coauthored more than 150 refereed journal and conference articles in the areas of analog and RF circuit design. He holds seven patents on RF circuits. His current research interests include integrated transceiver circuits for 5G and beyond wireless applications.



**Marko Fleischer** received the Diploma degree in electrical engineering (EE) from TU Dresden, Dresden, Germany, in 1996.

In 1990, he was working in the defense industry and joined Siemens Mobile Communication in 2000. Since 2000, he has been involved in the development of New Radio concepts ranging from active to passive intermodulation cancellation methods (AIM/PIM/SIC), studies of 5G full duplex, and OFDM radar. He is currently with Nokia RF System Engineering, Ulm, Germany.



**Mikko Valkama** (S'00–M'01–SM'15) received the M.Sc. and D.Sc. degrees (Hons.) in electrical engineering (EE) from the Tampere University of Technology (TUT), Tampere, Finland, in 2000 and 2001, respectively. His Ph.D. dissertation was focused on advanced I/Q signal processing for wideband receivers: models and algorithms.

In 2003, he was a Visiting Post-Doctoral Research Fellow with the Communications Systems and Signal Processing Institute, San Diego State University (SDSU), San Diego, CA, USA. He is currently a Full Professor and the Department Head of Electrical Engineering with Tampere University (TAU), Tampere. His current research interests include radio communications, radio localization, and radio-based sensing, with particular emphasis on 5G and beyond mobile radio networks.

Dr. Valkama was a recipient of the Best Ph.D. Thesis Award of the Finnish Academy of Science and Letters for his Ph.D. dissertation.